

A scenario for ultra-diffuse satellite galaxies with low velocity dispersions

Adi Nusser ^{*}

Department of Physics and the Asher Space Research Institute, Israel Institute of Technology Technion, Haifa 320003, Israel

25 May 2022

ABSTRACT

A scenario for achieving a low velocity dispersion for the galaxy NGC1052-DF2 and similar galaxies is presented. A progenitor galaxy of total mass $\lesssim 5 \times 10^{10} M_{\odot}$ infalling onto a Milky Way-size host undergoes tidal stripping and additional episodes of star formation, possibly enhanced by the action of the tidal gravitational field. Gas removal by supernova feedback, assisted by tidal stripping, leads to a substantial reduction of the velocity dispersion of stars within one effective radius. In this framework, the observed stellar content of NGC1052-DF2 is associated with a progenitor mass close to that inferred from the global stellar-to-halo mass ratio. As far as the implications of kinematics are concerned, even if at a ~ 20 Mpc distance, it is argued that NGC1052-DF2 is no more peculiar than numerous early type galaxies with seemingly little dark matter content.

Key words: galaxies: halos - cosmology: theory, dark matter, galaxies

1 INTRODUCTION

The dark matter (DM) is subdominant within the effective radii (enclosing half the total light) R_e of ordinary early type galaxies (ETG) (c.f. Cappellari 2016, for a review). The inferred average DM fraction within R_e is $\sim 30\%$ and a fraction of these galaxies is even consistent with no DM at all in those inner regions. These findings are obtained using analyses of the stellar kinematics as well as gravitational lensing (e.g. Treu & Koopmans 2004; Mamon & Lokas 2005a; Auger et al. 2009; Thomas et al. 2011). Outer parts of ETGs extending to several R_e could be directly probed with the kinematical measurements of planetary nebulae (PN) detectable through strong emission lines. While it is reasonable that the stellar kinematics in the inner regions is only mildly dominated by DM, a puzzle emerged when galaxies with PN kinematics required very little DM also in the outer regions (Romanowsky et al. 2003). However, a high DM content has been demonstrated to reproduce the observed low velocity dispersion of PNs in a realistic scenario for the formation of ETGs, where the PNs are expected to follow elongated orbits.

The global stellar-to-halo-mass ratio (SHMR) (Behroozi et al. 2010; Moster et al. 2013; Rodríguez-Puebla et al. 2017) can be used to derive halo virial masses, M_h , from the observed stellar masses, M_* . Assuming DM halos with an NFW density profile (Navarro et al. 1996), the virial mass tuned to match the stellar kinematics of SDSS ellipticals yields $M_h/M_* \sim 3$ (with a large scatter) in galaxies with $M_* \sim 5 \times 10^{10} M_{\odot}$ (see figure 10 in Padmanabhan et al. 2004), a factor ~ 40 lower than the global SHMR. Seen in this light and given the difficulty in inferring the virial

mass from the kinematics of the inner region alone (e.g. Mamon & Lokas 2005b), it is surprising that the ultra-diffuse galaxy (hereafter UDG) NGC1052-DF2 has attracted a great deal of attention as a galaxy with little DM.

The stellar velocity dispersion, σ_* , in NGC1052-DF2 has been measured separately by (Emsellem et al. 2018) using the MUSE integral-field spectrograph at the (ESO) Very Large Telescope and by (Danieli et al. 2019) with the Keck Cosmic Web Imager (KCWI). The velocity dispersion measurements are sufficiently different that they could lead to contrasting implications regarding the mass of the galaxy. Assuming NGC1052-DF2 is at a distance $D = 18$ Mpc, the value $\sigma_* = 8.5_{-3.1}^{+2.3} \text{ km s}^{-1}$ derived by Danieli et al. (2019) yields a dynamical mass $M(< 1.3R_e) = (1.3 \pm 0.8) \times 10^8 M_{\odot}$. However, Emsellem et al. (2018) obtain $\sigma_* = 10.8_{-4}^{+3.2} \text{ km s}^{-1}$, giving $M(< 1.8R_e) = 3.7_{-2.2}^{+2.5} \times 10^8$ and a factor of 1.6 smaller for $M(< R_e)$. By extrapolating the estimate $M(< 1.8R_e)$ of Emsellem et al. (2018) out to the virial radius using the NFW density profile, we obtain a virial mass $M_h \approx 1.4_{-1}^{+2} \times 10^9 M_{\odot}$ for a concentration parameter $c = 14$ and $M_h = 2.7_{-2.1}^{+5.2} \times 10^9 M_{\odot}$ for $c = 7$. For the stellar mass $M_* \sim 1.6 \times 10^8 M_{\odot}$ of NGC1052-DF2, the standard SHMR¹ implies $M_h \sim 6 \times 10^{10} M_{\odot}$, significantly larger than M_h obtained by an extrapolation of $M(< 1.8R_e)$, even using the value in Emsellem et al. (2018). This mismatch between the SHMR and kinematical mass inference undoubtedly bears a close similarity to the situation of ETGs discussed above.

¹ In the case of satellite galaxies, the SHMR gives the virial mass of the progenitor prior to any tidal stripping by the gravitational field of the host galaxy.

* E-mail: adi@physics.technion.ac.il

The current paper offers a dynamical scenario which accommodates a high M_h for the progenitor galaxy with the observed stellar kinematics of NGC1052-DF2. We extend the idea presented in Nusser (2019) dealing with the kinematics of 10 globular clusters (GCs) in NGC1052-DF2 (van Dokkum et al. 2018a). In addition to stripping of outer parts of the galaxy by the action of external gravitational tides, the current work explores the dynamical consequences of gas ejection by energetic feedback from supernovae.

As in any dynamical modeling, the distance is needed to set the spatial physical scale. There are two distance estimates in the literature, Trujillo et al. (2019) derive a distance $D \approx 13$ Mpc, while van Dokkum et al. (2018b) report $D = 18.7 \pm 1.7$ Mpc. The nearer distance leads to a smaller stellar mass ($\sim 6 \times 10^7 M_\odot$) and, thus, brings NGC1052-DF2 closer to the standard SHMR (Trujillo et al. 2019). Therefore, the main interest is in the mass models for $D = 18$ Mpc and here we present results for this distance only.

We define the virial radius r_v to be the radius of the sphere within which the mean halo density is 200 times the critical density $\rho_c = 3H_0^2/8\pi G$. We adopt cosmological parameters based on the recent Planck collaboration (Planck Collaboration et al. 2018). Throughout we take the Hubble constant $H_0 = 67.8 \text{ km s}^{-1} \text{ Mpc}^{-1}$ and the baryonic and total mass density parameters $\Omega_b = 0.049$ and $\Omega_m = 0.311$.

The outline of the remainder of the paper is as follows. The analysis relies on numerical simulations run under the assumption a spherical configuration. The numerical set-up and the modelled baryonic processes are described in §2. The inferred prediction for the line of sight velocity dispersion and comparison with the observed dispersion is presented in §3. We conclude with a summary and a discussion in §4.

2 THE SET-UP

We start with a progenitor (satellite) halo of virial mass M_h of a few times $10^{10} M_\odot$ at the outskirts of a larger parent galaxy at redshift $z \sim 2$. Since the cooling time in this halo mass range is short compared to the dynamical time (e.g. White & Frenk 1991), assume that a significant gas fraction has already cooled and settled well inside the virial radius. In accordance with observations (Behroozi et al. 2013) and simulations of galaxy formation (Garrison-Kimmel et al. 2019), we also assume that at this stage only a fraction $\lesssim 0.2$ of the final stellar mass has formed². As the (gas rich) satellite orbits into the parent halo, it begins to lose matter from its outer parts by the tidal gravitational forces of the parent halo. It also continues to form stars accompanied by supernova (SN) explosions, perhaps at a boosted rate due to tidal interactions with the host halo (Martig & Bournaud 2008; Renaud et al. 2014). Because the gravitational potential depth in the satellite halos we consider corresponds to circular velocities $V_c \lesssim 60 \text{ km s}^{-1}$, SN feedback is sufficient for the removal significant amounts of gas away from the gravitational grip of the halo (Larson 1974; Dekel & Silk 1986; Munshi et al. 2013). This is consistent with the fact that the UDG NGC1052-DF2 is extremely gas poor (Chowdhury 2019; Sardone et al. 2019). Another mechanism for gas removal could be ram pressure exerted by the diffuse gas in the parent halo. Continuous star formation activity could lead to slow removal of gas on time scales longer than the dynamical time of the system, while a star burst and ram pressure

could cause a fast ejection of the gas. In a slow gas removal, the halo DM particles remain in a quasi-steady state. In contrast, in a fast ejection process the DM particles momentarily maintain their velocities, while gaining (positive) potential energy. After a few dynamical times, the system relaxes to a new equilibrium which, in general, is different from the steady state reached at the end of a slow gas removal process (e.g. Pontzen & Governato 2012; Dutton et al. 2016).

2.1 The Numerical Scheme

Under the assumption of a spherically symmetric configuration, we simulate the dynamical effects of cooling, stripping and gas ejection. Only the collision-less particles are “live” and move self-consistently under the action of their own gravity as well as that of the stellar and cool gas components. The gravitational force field of these baryonic components is computed assuming they follow the density profile of the observed stellar component, but with a mass that varies with time according to the cooling and galactic wind recipes described below. Thus the distinction between the stars and the cool gas is unimportant dynamically and, at times, we shall refer to them as accreted baryons.

Initially, the collision-less particles represent the DM and the hot gas, where the latter is assumed to follow the density distribution of the DM halo. The collision-less particles are treated as spherical shells moving under the gravitational force field of the monopole term of the mass distribution computed relative to the halo center (as defined in the initial conditions). The self-gravity of the collision-less particles is derived following White (1983), with a force Plummer softening of length of 10 pc.

The numerical scheme aims at modelling the dynamical consequences of the following processes:

- I. **Gas cooling:** the mass of the cool gas, M_g , is increased linearly from zero to $M_g = f_g M_h$ in the time period from $t_{C1} = 1$ to $t_{C2} = 2$ Gyr. The parameter $f_g = \Omega_b/\Omega_m$ is the gas fraction of the total halo mass. The mass of each collision-less particle is accordingly reduced by a factor $1 - M_g(t)/M_h$. The distribution of the cool mass, $M_g(t)$, is set according to the density profile of the observed stellar profile described below.
- II. **Trimming/Stripping:**
 - a. *Linear:* Collision-less particles lying at time t beyond a trimming radius $r_{tr}(t)$ are excised from the simulations, where $r_{tr}(t)$ varies linearly from $r_{tr} = r_v$ at $t_{tr1} = t_{C2} = 2$ Gyr to $r_{tr} = 10$ kpc at $t = t_{tr2} = 4$ Gyr.
 - b. *Dynamical tidal stripping:* the actual gravitational field of the parent halo is included in the simulation. The satellite is assumed to move on a circular orbit and the equations of motion are solved in the non-inertial frame rotating with the satellite, taking into account the Coriolis and centrifugal forces in addition to the gravity of the parent halo. As before, the gravitational force of the satellite is computed assuming spherical symmetry with respect to its centre. The approximation of spherical symmetry is unrealistic for the already stripped particles forming galactic streams. However, the dynamics of those particles is irrelevant to us.
- III. **Galactic winds:**
 - a. *Fast:* a mass $M_g = f_g M_h - M_*$, where M_* is the observed mass of the stellar component, is suddenly removed from the accreted baryons at $t = t_{w1} = t_{w2} = 4$ Gyr. The remaining

² All we care about is that the SN feedback from stars forming at later times is sufficient to remove the gas from the galaxy. See the Appendix.

mass M_* is fixed thereafter and represents the observed stellar component.

- b. *Slow*: a mass $M_g = f_g M_h - M_*$ is removed linearly with time between $t = t_{w1}$ and $t_{w2} = 8$ Gyr.

For reference, the period of a circular orbit of radius (in kpc) r_{kpc} is $t_c = 2\pi(r_{\text{kpc}}^3/GM)^{1/2} = 0.3(r_{\text{kpc}}^3/M_8)^{1/2}$ Gyr where M_8 is the mass (in $10^8 M_\odot$) within r_{kpc} . For $M \sim 10^8 M_\odot$ at $r \sim 2$ kpc giving $t_c \sim 0.85$ Gyr for the orbital period of a circular orbit at $r \sim 2$ kpc inside NGC1052-DF2. The circular orbital period in the parent galaxy is $t_c^{\text{DF2}} \sim 2.5(R_{100}/V_{250})$ Gyr, where we R_{100} is the orbital radius in 100 kpc and V_{250} is the velocity in 250 km s^{-1} .

The approach outlined above is obviously quite limited in comparison to 3D simulations of galaxy formation, but it has the advantage that the dynamical consequences of the baryonic processes can easily be assessed and discerned. Full 3D simulations including gas process, star formation and feedback are more realistic but they suffer from uncertain complex sub-grid modelling and are substantially harder to analyse.

2.2 The stellar density profile

We describe the 3D density distribution of the observed stellar component in terms of an Einasto profile

$$\rho_*^E = \rho_0 \exp \left[- \left(\frac{r}{h} \right)^{1/n} \right], \quad (1)$$

where $n = 0.649$, $h = r_{-2}/(2n)^n$, $r_{-2} = 2.267$ kpc and ρ_0 and ρ_0 is tuned to yield the total mass. This profile yields a good fit to the 2D Sérsic profile representing the observed surface brightness with $R_e = 2$ kpc (for $D = 18$ Mpc) and a Sérsic index $n = 0.6$ (van Dokkum et al. 2018a). The stellar mass is normalized to $1.6 \times 10^8 M_\odot$. The left panel of Fig. 1 plots the Sérsic profile as a function of the projected distance, R , together with the surface density obtained by integrating the Einasto profile along the line of sight out to a maximum 3D radius of 10 kpc. The agreement between the two profiles is excellent. To the right we show the mass enclosed in cylinders of radius R for these two profiles. In addition, we show here the 2D mass obtained with an NFW profile of virial mass $M_h = 10^{10} M_\odot$ and $c = 9$ pruned at a 10 kpc 3D distance.

2.3 Derivation of the stellar velocity dispersion

Our goal is predicting the line of sight velocity dispersion as a function of the projected distances. The simulations provide the total gravitational force field (per unit mass), $g(r)$, resulting from the DM and baryonic components. Since the stellar component is represented in terms of a fixed density profile, we resort to the Jeans equation in order to derive the velocity dispersion of the stars.

Let $\sigma_r^2(r) = \langle v_r^2 \rangle$ be the stellar velocity dispersion in the radial direction at distance r from the center of the galaxy. The velocity anisotropy ellipsoid is described by the parameter $\beta(r) = 1 - \sigma_t^2/2\sigma_r^2$ where $\sigma_t^2 = \sigma_\phi^2 + \sigma_\theta^2$ is the velocity dispersion in the direction tangential to r . The Jeans equation for a steady state distribution of stars is

$$\frac{dn\sigma_r^2}{dr} + \frac{2\beta}{r}n\sigma_r^2 = -ng \quad (2)$$

where $n = n(r)$ is the known number density of stars at r . Assuming β is independent of r , the solution to this equation is

$$\sigma_r^2 = -\frac{1}{n(r)r^{2\beta}} \int_r^\infty n(r') r'^{2\beta} g(r') dr'. \quad (3)$$

There is no restriction on β in the expressions above, but there is no guarantee that a particular β actually corresponds to any physical system described by a steady state phase space distribution function (DF). Indeed, numerical integration of Eddington's formula did not yield a non-negative isotropic DF (i.e. $\beta = 0$) (c.f. the discussion in §4.3.1 in Binney & Tremaine 2008) that describes the observed stellar distribution (modelled as an Einasto profile) in equilibrium under its self-gravity and the gravity of an NFW halo. For $\beta < -0.01$, models of the form $f(E) = L^{-2\beta} f_1(E)$ are numerically found to be consistent with the desired configuration. We thus restrict ourselves to negative β^3 .

We choose the line of sight to lie in the z -direction. The velocity dispersion, $\sigma_z^2 = \langle v_z^2 \rangle$, at a point R and z is

$$\sigma_z^2 = \sigma_r^2 (1 - \beta \sin^2 \theta), \quad (4)$$

where $\sin \theta = R/\sqrt{R^2 + z^2}$. The observed parallel velocity dispersion at a projected distance R is

$$\sigma_u^2 = \frac{1}{\int_{-\infty}^{\infty} dz n(z, R)} \int_{-\infty}^{\infty} dz n(z, R) \sigma_z^2. \quad (5)$$

In comparisons with the observed velocity dispersion, we show (unless stated otherwise) results after averaging σ_u^2 over the stellar surface density within R .

3 RESULTS

The initial mass in stars and cool gas in the progenitor satellite is set to zero and the initial positions and velocities of the collisionless particles are sampled from an ergodic (i.e. isotropic) phase space DF. The DF is numerically derived from the NFW density profile by integrating the Eddington relation. This DF is a monotonic function of energy and thus the system is stable (Binney & Tremaine 2008). The simulations are run for a period of 9.7 Gyr using the leapfrog integration scheme. In order to reduce effects related to the finite number of particles, the simulations are first run for 1 Gyr, before the sequence of baryonic processes is implemented (I–III above). The energy conservation of the code for 10^6 self-gravitating collisionless particles alone is better than 1 part in 10^4 .

We will present results for two values of for the virial mass, $M_h = 10^{10} M_\odot$ and $5 \times 10^{10} M_\odot$. The virial radius and circular velocity corresponding to $M_h = 10^{10} M_\odot$ are 46 kpc and 31 km s^{-1} , respectively. We consider two values of the concentration parameter, $c = 9$ and 13. Using the Ludlow et al. (2016) recipe for calculating the halo concentration versus halo mass (hereafter, the c – M relation), the mean concentration for halos of this mass is $c = 12.4$. The value $c = 9$ is within the 1σ scatter of the expected variations of c in relaxed halos (see Fig. 5 in Hellwing et al. 2016) and is motivated by the analysis of Nusser (2019), which found that the GC kinematics prefers smaller concentrations. For the the larger mass halo $5 \times 10^{10} M_\odot$ we consider $c = 8$ and $c = 11$, where the c – M relation gives $\bar{c} = 11.1$ and $c = 8$ is within the 1σ scatter. For this halo, the virial radius 78 kpc and the circular velocity is 53 km s^{-1} . The number of collisionless particles in the simulations with the high and low mass halo is 10^7 and 10^6 , respectively.

³ Including only the self-gravity of the stellar component allows for an isotropic and non-negative DF. But for $\beta > 0$, the models $f(E) = L^{-2\beta} f_1(E)$ lead to negative f .

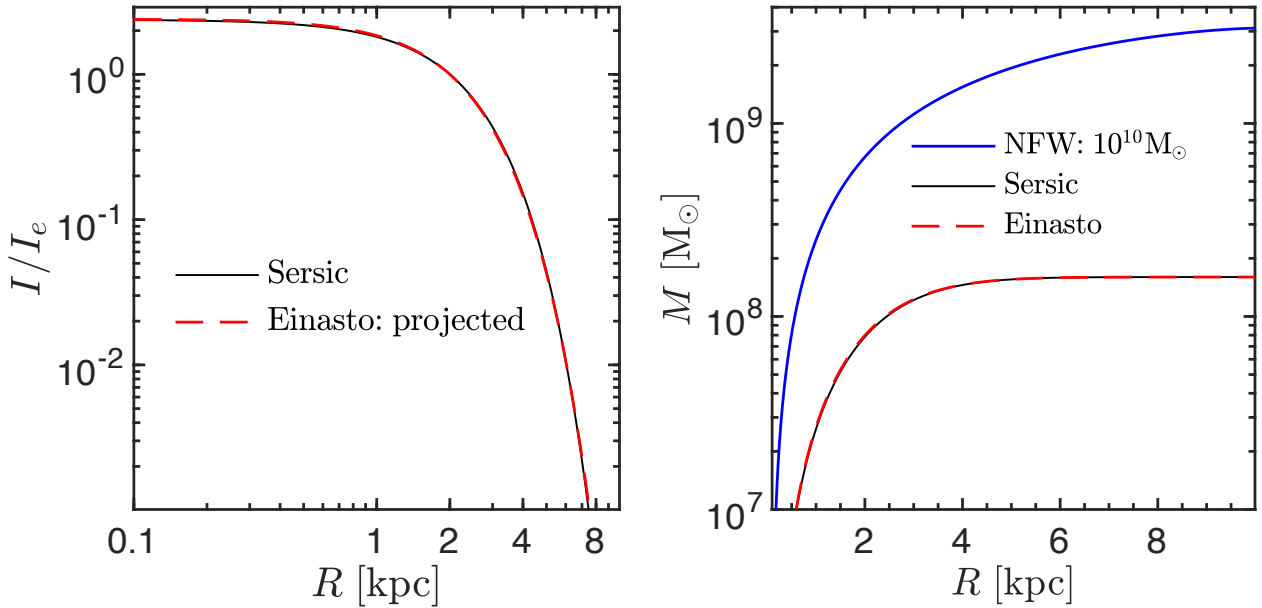


Figure 1. *Left:* The stellar surface density versus projected distance R . The Sérsic fit to the observed NGC1052-DF2 stellar distribution is shown as the solid black line, while the overlapping dashed red line is the projected 3D Einasto profile truncated at 10 kpc. *Right:* Stellar mass within 2D cylinders versus R . The solid blue line correspond to an NFW halo with $M_h = 10^{10} M_\odot$ and $c = 9$ truncated at 10 kpc.

3.1 Small halo

We begin with $M_h = 10^{10} M_\odot$. Using the Jeans equation, we calculate σ_u from the simulation output as described in §2.3. Fig. 2 plots curves of σ_u versus the projected distance R for $c = 9$ (left column) and $c = 13$ (right), Each group of curves corresponds to 4 values of β , as indicated in the middle row panels. The group of black curves in the top row panels are computed from the simulations at $t = 1$ Gyr (black curves), just before gas cooling is switched on, as described in §2.1. At this stage, neither the stellar nor the cool gas component have formed, but we still compute σ_u for a population of “massless” tracers distributed according the observed density profile ρ_*^E given in Eq. 1. The diamond and open circle with attached error bars represent the observed velocity dispersions from (Danieli et al. 2019) and (Emsellem et al. 2018), respectively. This figure refers to results without any trimming/stripping.

At 2 Gyr (blue curves, top panels), the cooling phase ended with a cool gas mass $M_g = (\Omega_b/\Omega_m)M_h = 1.55 \times 10^9 M_\odot$ assumed to follow the form ρ_*^E . There is a significant enhancement of σ_u as a result of the transfer of mass from the collision-less particles to the more centrally concentrated baryonic component. During the period 2-4 Gyr, the baryonic component remains the same and since no trimming is invoked, the distribution of the collision-less particles essentially remains the same.

The red curves in middle panel show σ_u just after an event of fast wind ejecting in a single burst a mass $M_g - M_* = 1.39 \times 10^9 M_\odot$ corresponding to all available cool gas after leaving behind the stellar component with $M_* = 1.6 \times 10^8 M_\odot$. In the same panels, the blue curves correspond to a slow wind lasting until $t_{w2} = 8$ Gyr (see III.b in §2.1). Since the slow wind begins at $t_{w2} = 4$ Gyr, the blue curves in the middle and top panels are almost identical with small differences entirely due to fluctuations in the distribution of the collision-less particles.

By $t = 9.7$ Gyr, the system reaches a steady steady with a galaxy made of DM collision-less particles in addition to stellar

component of mass M_* . The results for $c = 9$ in the bottom panel on the left indicate that steady state is sensitive to the gas removal mode. The fast wind is more efficient at bringing the velocity dispersion to a comfortable agreement with the observations. As evident in the bottom panel in the column to the right, for the larger concentration, $c = 13$, the final σ_u is consistent with the measured dispersion at about the 2σ level for $\beta = -1$ and $\beta = -1.5$. For this more concentrated halo, the two wind modes yield roughly similar results.

Fig. 3 explores the effect of linear trimming (II.a in §2.1). For brevity, the plot shows the results in the steady state limit at $t = 9.7$ Gyr. Trimming has very little effect on σ_u for the simulations with $c = 9$, as readily seen by comparing this figure and the bottom panel in the previous figure. For $c = 13$, the effect of trimming is more pronounced for the fast wind mode, while almost negligible for slow wind. To understand this behaviour we inspect, in Fig. 4, the actual density profile for various cases. The solid and dashed curves in blue ($c = 9$) correspond to densities of DM particles at the final time for untrimmed and trimmed simulation runs, respectively. The curves almost overlap out to $r = 4$ kpc and are below the observed stellar density (dotted cyan) in the range 2-5 kpc. This explains why both trimming almost has no effect on σ_u for $c = 9$. However, for $c = 13$ the red curves deviate at $r \gtrsim 1$ kpc and both are above the observed stellar density. The same conclusions can be reached from Fig. 5 showing the mass within a radius r . The differences in $M(r)$ between the trimmed and the untrimmed simulations is clearly more pronounced for $c = 13$ (red) than $c = 9$ (blue).

3.2 Large halo

We now turn to the larger halo with $M_h = 5 \times 10^{10} M_\odot$. In this case, the gas mass that can collapse to the inner regions is 5 times larger than in the $10^{10} M_\odot$ halo. Thus, despite the deeper potential well ($V_c = 52 \text{ km s}^{-1}$ compared to 31 km s^{-1}), the fraction of gas

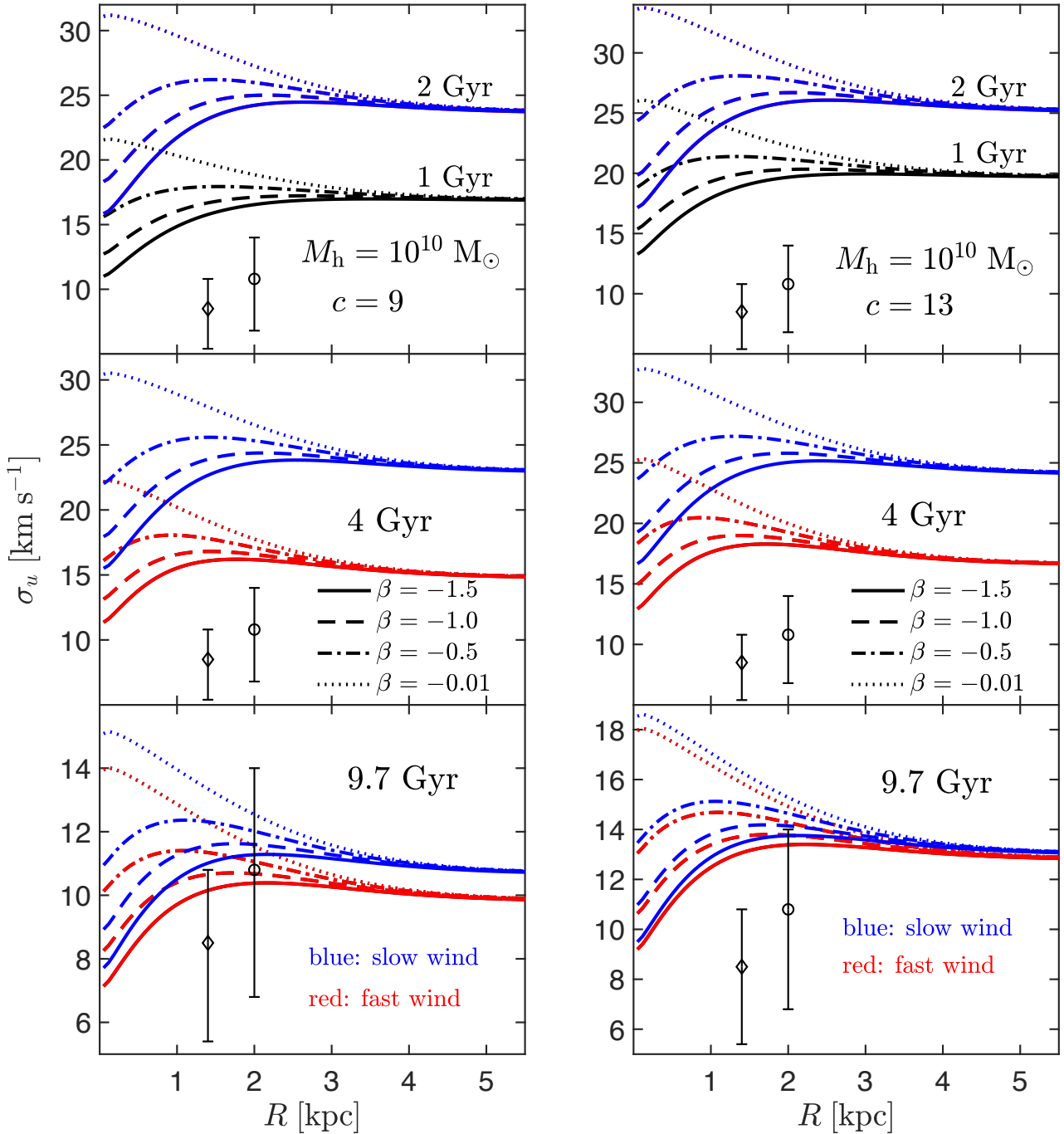


Figure 2. The l.o.s velocity dispersion versus projected distance obtained from the simulations with virial halo mass $M_h = 10^{10} M_\odot$ and $c = 9$ (column to the left) and $c = 13$ (to the right). Each group of 4 curves represent 4 values of the velocity anisotropy parameter, β , as indicated in the middle row. Red and blue correspond to fast and slow winds, respectively. At $t = 2$ Gyr, the red and blue curves overlap. The black curves in the top panel shows results at 1 Gyr just before the gas is collapsed. Shown are results from simulations without tidal stripping/trimming.

to original DM mass within 10 kpc is actually larger than in the smaller halo, 1.02 versus 0.514 for $M_h = 10^{10} M_\odot$ with $c = 9$.

The results are shown in Fig. 6 for the fiducial cool gas mass fraction, $f_g = M_g/M_h = \Omega_b/\Omega_m = 0.155$ and also for nearly half this value, $f_g = 0.07$. To avoid cluttering of the figure we show results obtained with $\beta = -1.5$ only and simply point out that at $R \approx 0$, the velocity dispersion for $\beta = -0.01$ is nearly a factor of 2 larger than $\beta = -1.5$. The cyan solid line corresponds to $c = 11$ falling on the $c-M$ relation (Ludlow et al. 2016), while all other

lines are for $c = 8$. The bottom panel demonstrates that the ejection of the relatively large amount of gas for $f_g = 0.155$ brings down σ_u (dash dotted) to a level completely consistent with the observations for $c = 8$. The agreement with the observed σ_u is even better than the corresponding $\beta = -1.5$ curve plotted the bottom panel in Fig. 2 for the lower mass $M_h = 10^{10} M_\odot$. Like in the lower mass case, the concentration parameter plays an important role. Comparing between the cyan solid and the red dash-dotted lines, the velocity dispersion for $c = 11$ is nearly %50 higher than

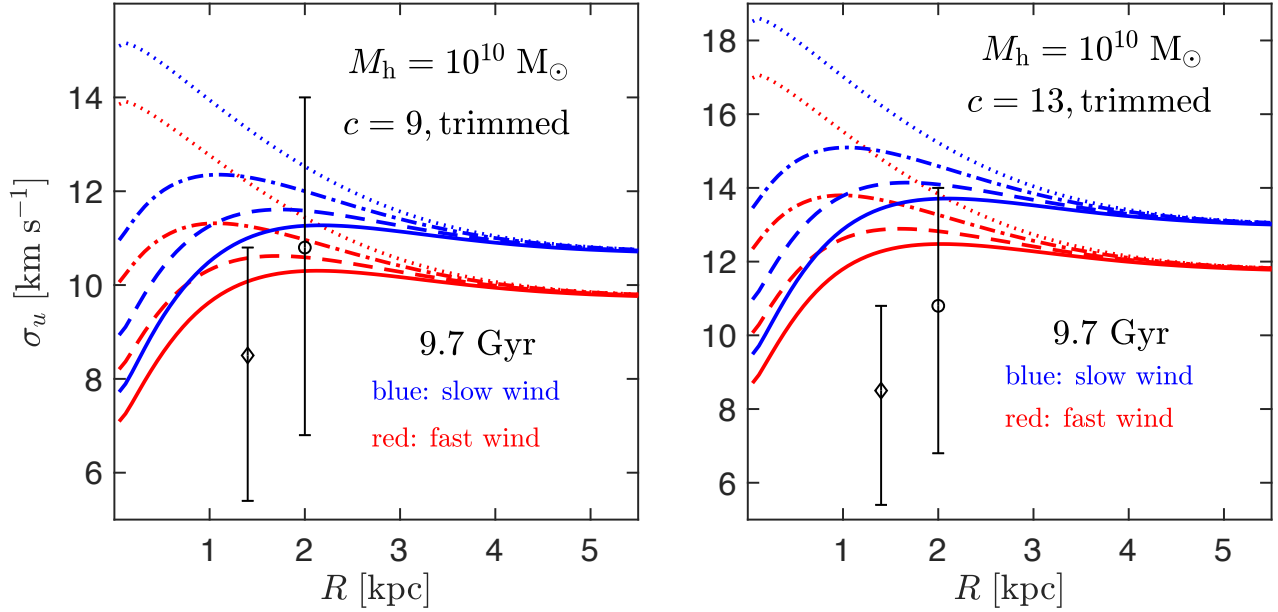


Figure 3. The same as the bottom panels in the pervious figure but for the simulations with trimming.

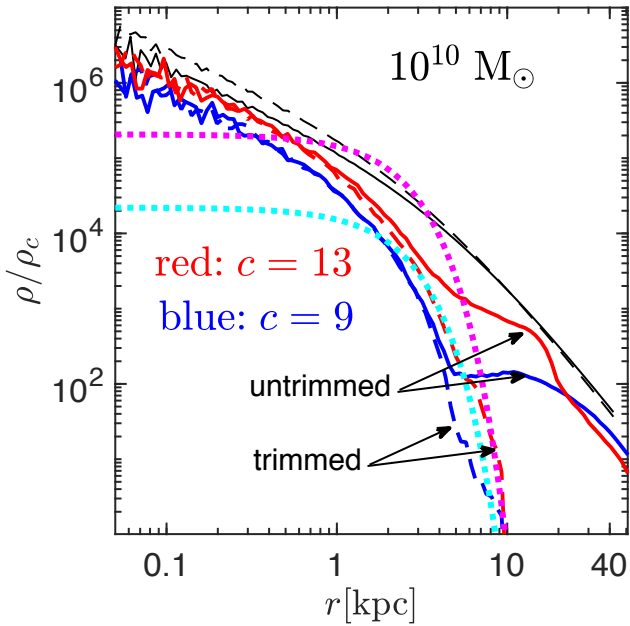


Figure 4. Density profiles (in units of the critical cosmic density) obtained from the simulations with fast wind for $M_h = 10^{10} M_\odot$. Dashed and solid thick black are the DM density profiles, respectively, for $c = 13$ and $c = 9$, at $t = 1$ Gyr just before turning on gas cooling. The DM profiles at $t = 9.7$ Gyr without trimming are thick solid where the red is for $c = 13$ and blue for $c = 9$. The thick dashed curves are the same as the solid but for simulations with linear trimming. The dotted blue curve is the stellar profile at the final time, while the dotted red is the baryonic density profile at $t = 2$ Gyr, i.e. the maximum value reached by M_g .

$c = 8$ at $t = 9.7$ Gyr. The following conclusions are also valid for $c = 11$, but for clarity of the figure we only plot results for $c = 8$. For $f_g = 0.155$, the trimmed and untrimmed simulations, yield very similar σ_u . Therefore, only the trimmed results are pre-

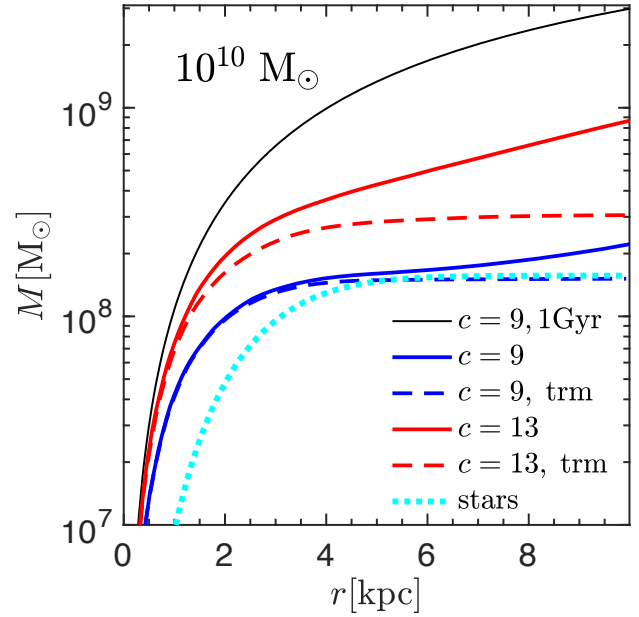


Figure 5. Mass enclosed in a 3D radius r for several of the density profiles from the previous figure.

sented in Fig. 6. In contrast, for $f_g = 0.07$, trimming has a significant effect on the final σ_u as revealed by the comparison between the dotted (trimmed) and dashed (untrimmed) curves in the bottom panel. It is intriguing, however, the two curves are almost identical at the earlier time, $t = 4$ Gyr, as shown in the middle panel (small differences can be seen by inspecting the actual numerical value). To understand this behavior, we plot in Fig. 7 the density profiles obtained with $f_g = 0.07$. At 4 Gyr, the trimmed (blue dashed) and untrimmed (red solid) almost completely overlap out to $r = 3$ kpc. The red dotted curve shows the baryons (cool gas + stars) density

just before ejection by fast wind just before 4 Gyr. Thus, between 1 kpc and 8 kpc the baryons are actually dominant until gas removal.

For $c = 8$, even the smaller f_g (dotted magenta) yields a reasonable agreement with the observations at less than a 2σ deviation from the [Danieli et al. \(2019\)](#) measurement (diamond symbol). Note that the At 2 Gyr (top panel), gas contraction with the larger f_g boosts σ_u to higher values than low f_g . At 9.7 Gyr (bottom panel), the situation is reverse with the large f_g having lower σ_u . This is due to the more substantial reduction in the total gravity as a result of removal of a larger amount of gas. For $f_g = 0.07$ and $c = 11$ (not shown), the value of σ_u reaches 14 km s^{-1} at $R \approx 2$.

So far we have considered the linear trimming recipe III.a in §2.1. It is prudent to explore whether this recipe mimics, at least approximately, a realistic stripping by the gravitational fields of a host halo. For this purpose, we apply the dynamical recipe III.b assuming the satellite moves on a circular orbit of radius 300 kpc in the gravitational field of an NFW host halo of virial mass $2.9 \times 10^{12} M_\odot$ and $c = 8$. We run the simulation for the large mass case $M_h = 5 \times 10^{10} M_\odot$ with $c = 8$, where the equations of motion are written and numerically solved in the non-inertial frame attached to the satellite. As we already have found for the linear trimming recipes, the corresponding dynamical effects are more pronounced for the low gas fraction $f_g = 0.07$. Hence, the simulation with dynamical trimming is run with this gas fraction. Curves of σ_u from the simulation output at 9.7 Gyr are plotted in red in Fig. 8. Also plotted, in blue, are the results from the linear trimming obtained previously (see Fig. 6). It is reassuring that the two recipes yield similar results but perhaps not surprising since in both cases the stripped matter is well outside R_e . Given the approximate nature of the analysis here, we do not make any further attempt to tune the parameters of the host halo in order to bring the dynamical trimming even close to the linear trimming. The agreement seen in the figure is quite satisfactory for our purposes.

3.3 Velocity dispersion at larger distances: the globular clusters

We briefly discuss the agreement between the scenario presented here and the kinematical observations of GCs in NGC1052-DF2. For these tracers, individual velocity measurements are available ([van Dokkum et al. 2018a](#)). Unfortunately, the number of these tracers is small and the errors are large. [Nusser \(2019\)](#) presented an analysis based on the full phase space DF under the assumption of tidal stripping, but without the inclusion of the effects of gas cooling/ejection. We do not intend to apply the DF analysis to the model of the current paper. Instead, we provide prediction for σ_u and contrast it with the GC measured velocities. This is done in Fig. 9 plotting σ_u obtained as described in §2.3, but with $n \propto r^{-2.3}$ which is consistent with the observed distribution of the GCs on the sky ([Trujillo et al. 2019; Nusser 2019](#)). The results are shown for 4 values of β , as indicated in the figure. Note that here we show predictions for $\beta = 0.5$, since a steady state DF of the form $L^{-2\beta} f_1(E)$ with $\beta = 0.5$ can be found. This is in contrast with the stellar distribution whose form did not allow for a DF of that form with a non-negative β . We do not perform a full statistical analysis, but it is evident that the curves of all plotted values of β are in reasonable agreement with the data.

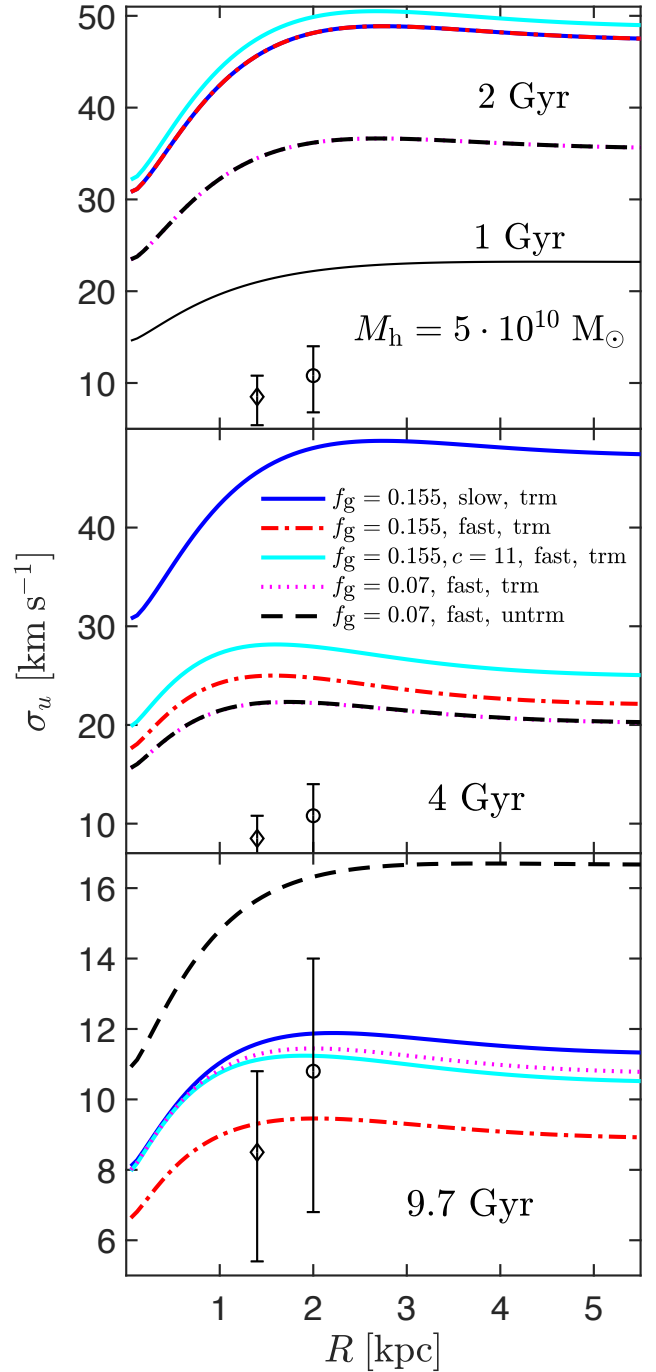


Figure 6. The l.o.s velocity dispersion from the simulations with $M_h = 5 \times 10^{10} M_\odot$ and $c = 8$, with the exception of the cyan solid line which is for $c = 11$. Only results for $\beta = -1.5$ are plotted. In the top panel, curves with the same f_g overlap. In the middle panel, just after fast gas ejection at 4 Gyr, despite the trimming, the curves with $f_g = 0.07$ are almost identical, but diverge by 9.7 Gyr as seen in the bottom panel.

4 SUMMARY AND CONCLUSIONS

Independent of how ultra-diffuse galaxies form ([Dalcanton et al. 1997; Amorisco & Loeb 2016; Di Cintio et al. 2017](#)), we have outlined steps through which a halo with $V_c \lesssim 100 \text{ km s}^{-1}$ can harbor a stellar component with a velocity dispersion $\sigma \ll V_c$. The proposed scenario relies on common assumptions regarding galaxy

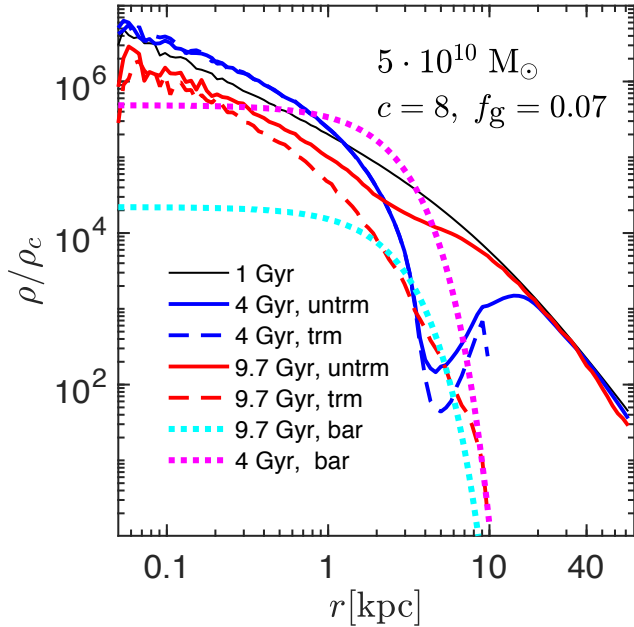


Figure 7. Density profiles from the simulations with $M_h = 5 \times 10^{10} M_\odot$ with $c = 8$ for fast winds. The dotted blue curve is the stellar profile at the final time, while the dotted red is the baryonic density profile at $t = 2$ Gyr, i.e. the maximum value reached by M_g .

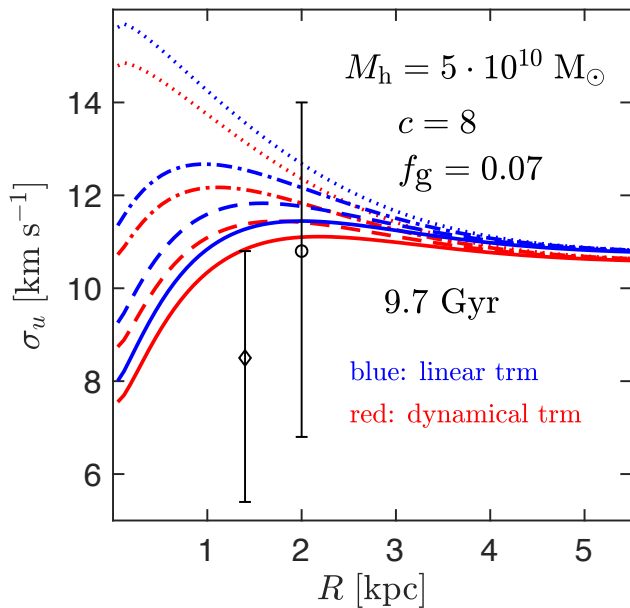


Figure 8. A comparison of the velocity dispersion obtained with linear and dynamical trimming recipes.

formation that when combined together can lead to galaxies with kinematics similar to NGC1052-DF2.

The scenario assumes the presence of an initial large cool gas fraction of the order of a few times the stellar mass, M_* . The assumption is supported by observational data for the range of stellar masses relevant for NGC1052-DF2 and NGC1052-DF4 (van Dokkum et al. 2019). Indeed, for optically selected galaxies with

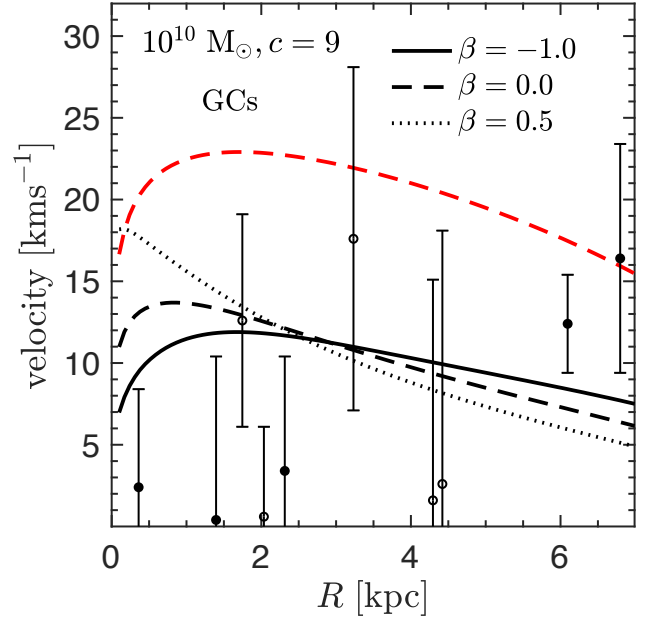


Figure 9. The l.o.s measured velocities of GCs versus R compared to the predicted σ_u at R (rather than the average within R as in all previous figures). The red curve is derived from the initial NFW profile with mass and concentration as indicated in the figure. The black curves are for the final output of the simulation with fast winds and no trimming.

$5 \lesssim M_*/10^7 M_\odot \lesssim 100$, Papastergis et al. (2012) find H I mass which could easily reach a factor of 10 larger than M_* .

An initially compact stellar component could be puffed-up by the shallowing of the potential well by gas ejection. The net outcome could be a diffuse stellar component with very low surface brightness (e.g. Di Cintio et al. 2017). The current work treated the stellar component in terms of a fixed density profile and did not explore this possibility. However, the details of this process in the context of low velocity dispersion galaxies, could be tested with simulations, also under the assumption of spherical symmetry, where the stellar component is treated as “live” collision-less particles following a suitable density profile. We leave that for a further study, where the sensitivity to the assumed initial stellar distribution is explored in detail.

It is possible to envisage the formation of completely DM free galaxies through galaxy collisions Silk (2019) or though the condensation in gaseous debris of galaxy mergers, as in the formation of tidal dwarf galaxies (e.g. Lelli et al. 2015). Both possibilities require fine tuning in order to produce the properties of a galaxy like NGC1052-DF2. In the current paper, we argue that there is nothing grossly unusual in the dynamics of this galaxy and that it is like many other galaxies which show weak evidence for dark matter.

The scenario favors a low halo concentration, but still within a reasonable deviation from the standard $c - M_h$ relation found in simulations. According to cosmological simulation, low concentrations are generally associated with more extended galaxies according to the relation Jiang et al. (2018)

$$r_e = 0.02 \left(\frac{10}{c} \right)^{0.7} r_v, \quad (6)$$

where r_e is the stellar half-mass radius. Taking $r_v = 78$ kpc ($M_h = 5 \times 10^{10} M_\odot$), the relation implies 1.45 kpc for $c = 11$, i.e. the mean c for that mass (Ludlow et al. 2016) and 1.8 kpc for $c = 8$.

Taking $c = 6$ which is about a 2σ deviation from the mean $c-M$ relation (Hellwing et al. 2016), we get $r_e = 2.23$, compared to the observed $r_e \approx 1.3R_e = 2.6$ kpc. Thus the lower concentration may also help increase r_e as desired for UDGs.

We have seen that tidal stripping helps in lowering the velocity dispersion in certain cases, but the main impact is caused by gas removal. Thus, in contrast to Ogiya (2018), we do not require a highly radial orbit of the satellite inside the host. Nonetheless, tidal forces of the host and also ram pressure can play an indirect role by enhancing star formation activity, increasing the chances for a fast gas removal mode.

In Nusser (2018), the author showed that orbital decay by dynamical friction of some of the GCs in NGC1052-DF2 is expected. The conclusion was based on simulations which included a dark halo. Dutta Chowdhury et al. (2019) have studied the dynamical friction in this system for the case of no dark matter at all. The presence of a core on in the 3D stellar distribution could suppress dynamical friction and even cause buoyancy (e.g. Cole et al. 2012). In addition scattering among GCs themselves helps keep the GCs afloat around the core at $r \sim 0.3R_e$. A serious shortcoming of that paper is that the GCs are treated as point masses and therefore they cannot address the disruptive effects of GC-GC scattering on the GCs themselves. Thus their findings should be taken with a grain of salt. Nonetheless, these authors confirm that dynamical friction is also important (e.g. figures 9& 10 in their paper), however, they argue that the observations can be reconciled by starting with a more spatially extended distribution of the GCs. They neither offer any quantitative assessment of the required initial conditions nor discuss of a realistic physical scenario in any detail. The proposal of starting a more extended GC distribution was also noted in Nusser (2018) as possible solution. The point was originally made by Angus & Diaferio (2009) as a potential solution to the Fornax dynamical friction conundrum (see also Boldrini et al. 2019). A detailed physical formation scenario for this type of initial conditions remains lacking. Thus, despite their odd conclusion regarding the consistent of the dynamical friction argument with observations, their actual findings actually agree with Nusser (2018).

ACKNOWLEDGEMENTS

This research was supported by the I-CORE Program of the Planning and Budgeting Committee, THE ISRAEL SCIENCE FOUNDATION (grants No. 1829/12 and No. 203/09).

REFERENCES

- Amorisco N. C., Loeb A., 2016, *MNRAS Lett.*, 459, L51
 Angus G. W., Diaferio A., 2009, *MNRAS*, 396, 887
 Auger M. W., Treu T., Bolton A. S., Gavazzi R., Koopmans L. V. E., Marshall P. J., Bundy K., Moustakas L. A., 2009, *ApJ*, 705, 1099
 Behroozi P. S., Conroy C., Wechsler R. H., 2010, *ApJ*, 717, 379
 Behroozi P. S., Wechsler R. H., Conroy C., 2013, *ApJ*, 770, 57
 Binney J., Tremaine S., 2008, *Galactic dynamics*. Princeton University Press
 Boldrini P., Mohayaee R., Silk J., 2019, *MNRAS*, 485, 2546
 Cappellari M., 2016, *ARAA*, 54, 597
 Chowdhury A., 2019, *MNRAS Lett.*, 482, L99
 Cole D. R., Dehnen W., Read J. I., Wilkinson M. I., 2012, *MNRAS*, 426, 601
 Dalcanton J. J., Spergel D. N., Summers F. J., 1997, *ApJ*, 482, 659
 Danieli S., van Dokkum P., Conroy C., Abraham R., Romanowsky A. J., 2019, *ApJ*, 874, L12

- Dekel A., Silk J., 1986, *ApJ*, 303, 39
 Dekel A., Woo J., 2003, *MNRAS*, 344, 1131
 Di Cintio A., Brook C. B., Dutton A. A., Macciò A. V., Obreja A., Dekel A., 2017, *MNRAS*, 466, L1
 Dutta Chowdhury D., van den Bosch F. C., van Dokkum P., 2019, *ApJ*, 877, 133
 Dutton A. A., Maccio A. V., 2014, *MNRAS*, 441, 3359
 Dutton A. A., et al., 2016, *MNRAS*, 461, 1
 Emsellem E., et al., 2018, *A&A*, 625, A76
 Garrison-Kimmel S., et al., 2019, Star formation histories of dwarf galaxies in the FIRE simulations: dependence on mass and Local Group environment (arXiv:1903.10515), <http://fire.northwestern.eduhttp://arxiv.org/abs/1903.10515>
 Hellwing W. A., Frenk C. S., Cautun M., Bose S., Helly J., Jenkins A., Sawala T., Cytowski M., 2016, *MNRAS*, 457, 3492
 Jiang F., et al., 2018, Is the dark-matter halo spin a predictor of galaxy spin and size? (arXiv:1804.07306), <http://arxiv.org/abs/1804.07306>
 Larson R. B., 1974, *MNRAS*, 169, 229
 Lelli F., et al., 2015, *A&A*, 584, 113L
 Ludlow A. D., Bose S., Angulo R. E., Wang L., Hellwing W. A., Navarro J. F., Cole S., Frenk C. S., 2016, *MNRAS*, 460, 1214
 Mamon G. A., Łokas E. L., 2005a, *MNRAS*, 362, 95
 Mamon G. A., Łokas E. L., 2005b, *MNRAS*, 363, 705
 Martig M., Bournaud F., 2008, *MNRAS Lett.*, 385, L38
 Moster B. P., Naab T., White S. D. M., 2013, *MNRAS*, 428, 3121
 Munshi F., et al., 2013, *ApJ*, 766
 Navarro J. F., Frenk C. S., White S. D. M., 1996, *ApJ*, 462, 563
 Nusser A., 2018, *ApJL*, 863, L17
 Nusser A., 2019, *MNRAS*, 484, 510
 Ogiya G., 2018, *MNRAS*, 480, L106
 Padmanabhan N., et al., 2004, *New Astron.*, 9, 329
 Papastergis E., Cattaneo A., Huang S., Giovanelli R., Haynes M. P., 2012, *ApJ*, 759, 138
 Planck Collaboration et al., 2018, eprint arXiv, 1807.06209
 Pontzen A., Governato F., 2012, *MNRAS*, 421, 3464
 Renaud F., Bournaud F., Kraljic K., Duc P.-A., 2014, *MNRAS: Lett.*, 442, 33
 Rodríguez-Puebla A., Primack J. R., Avila-Reese V., Faber S. M., 2017, *MNRAS*, 470, 651
 Romanowsky A. J., Douglas N. G., Arnaboldi M., Kuijken K., Merrifield M. R., Napolitano N. R., Capaccioli M., Freeman K. C., 2003, *Science (80-.)*, 301, 1696
 Sardone A., Pisano D. J., Burke-Spolaor S., Mascoop J. L., Pol N., 2019, *ApJ*, 871, L31
 Silk J., 2019, *MNRAS Lett.*, 488, L24
 Thomas J., et al., 2011, *MNRAS*, 415, 545
 Treu T., Koopmans L. V. E., 2004, *ApJ*, 611, 739
 Trujillo I., et al., 2019, *MNRAS*, 486, 1192
 White S. D. M., 1983, *ApJ*, 274, 53
 White S. D. M., Frenk C. S., 1991, *ApJ*, 379, 52
 van Dokkum P., et al., 2018a, *Nature*, 555, 629
 van Dokkum P., Danieli S., Cohen Y., Romanowsky A. J., Conroy C., 2018b, *ApJ*, 864, L18
 van Dokkum P., Danieli S., Abraham R., Conroy C., Romanowsky A. J., 2019, *ApJ*, 874, L5

APPENDIX A: SN FEEDBACK AND SHMR

Its is instructive to examine the SHMR as a function of the halo properties. According to Dekel & Silk (1986) (see also Dekel & Woo (2003)), the energy available for heating the gas as a result of SN forming through the formation of M_* mass in stars is

$$E_{\text{SN}} \sim M_* V_{\text{SN}}^2, \quad V_{\text{SN}} \sim 120 \text{ km s}^{-1}. \quad (\text{A1})$$

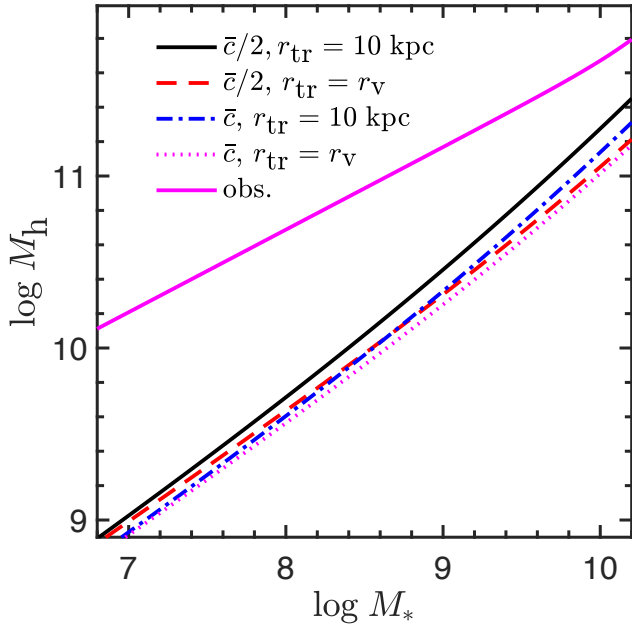


Figure A1. The halo virial mass versus stellar mass, computed according to Eq. A3, for different values of halo concentration and trimming radius, as indicated in the figure. The relation derived from the observations (Rodríguez-Puebla et al. 2017) is also plotted.

An upper bound on M_* is set by

$$E_{\text{SN}} \sim \frac{1}{2} M_{\text{g}} V_{\text{esc}}^2, \quad (\text{A2})$$

where V_{esc} is the escape speed of the gas from the halo to infinity. Taking $M_{\text{g}} = f_{\text{b}} M_{\text{h}} - M_*$ where f_{b} is the fraction of baryons of the total halo mass M_{h} , the last two equations give the SHMR

$$\frac{M_*}{M_{\text{h}}} \sim \frac{f_{\text{b}} V_{\text{esc}}^2}{2V_{\text{SN}}^2 + V_{\text{esc}}^2}. \quad (\text{A3})$$

Curves of M_{h} versus M_* computed according to this relation are plotted in Fig. A1 for several cases. In computing V_{esc} , the gas is assumed to escape to infinity from distance R_{c} given by Eq. 6.

The figure shows curves corresponding to two choices of the NFW concentration parameter as a function of halo mass, $c = \bar{c}(M)$ and $c = \bar{c}/2$ where $\bar{c}(M)$ is mean concentration-mass relation obtained from the fitting formula of Dutton & Maccio (2014) for halos identified in simulations. The value $c = \bar{c}/2$ is within 2σ scatter from \bar{c} as seen in halos identified in the simulations. Further, V_{esc} is computed for halos trimmed at $r_{\text{tr}} = 10$ kpc and $r_{\text{tr}} = r_{\text{v}}$. The solid magenta line, is the parametric relation derived from the observations in Rodríguez-Puebla et al. (2017). The difference between the various curves based on Eq. A3 is meagre compared to the observations. In all cases the curves lie more than one order of magnitude above the observed relation. At $M_* = 1.6 \times 10^8 M_{\odot}$, corresponding to the stellar mass of NGC1052-DF2, the observational relation yields $M_{\text{h}} = 6 \times 10^{10} M_{\odot}$, about an order magnitude above the curves predicted from Eq. A3. Assuming SN feedback is the only mechanism regulating star formation at the plotted mass range, the results imply that it is much more efficient than the estimation of Dekel & Silk (1986). One possibility for this mismatch is the assumption of a large filling factor of SN remnants in (Dekel & Silk 1986). The actual filling factor needed to regulate star formation may be substantially smaller than unity.